Journal of Zhejiang University-SCIENCE A (Applied Physics & Engineering)
ISSN 1673-565X (Print); ISSN 1862-1775 (Online)
www.jzus.zju.edu.cn; www.springerlink.com
E-mail: jzus@zju.edu.cn

Wall contact effects of particle-wall collision process in a two-phase particle fluid*

Shi-ming JI, Jiang-qin GE, Da-peng TAN†‡
(*Key Laboratory of E&M of Ministry of Education & Zhejiang Province, Zhejiang University of Technology, Hangzhou 310014, China*)
†E-mail: tandapeng@zjut.edu.cn

Received Jan. 20, 2017; Revision accepted Aug. 16, 2017; Crosschecked Nov. 7, 2017

Abstract: Particle-wall collision is a complex liquid-solid coupling matter approximating to a chaotic state. Previous research mainly focused on the issues of particle trajectory and near-wall flow field, but the particle-wall collision mechanism and contact effects are unclear. To address this, a coupled computational fluid dynamics and discrete element method (CFD-DEM) modeling method is proposed. Firstly, flow field profiles are acquired by the CFD method as the initial motion conditions. Then, the particles are regarded as rigid bodies, and the data interactions between CFD and DEM are implemented by calculating for interaction force and void fraction. The results show that there are radial texture phenomena on the particle trajectories caused by the flowing interference; the central region has the lowest velocity and can be regarded as the rigid core of a Rankine vortex; if inlet diameter is 20 mm, the contacting distribution with rotating superposition can reach the best uniformity; the higher viscosity can carry more particles, and the transporting ability of the fluid medium is improved; the uniform contact effects can be more easily performed by the low viscosity fluid. This research can offer theoretical relevance to the modeling for multi-phase particle fluid, and provide technical support for flow regulation in the areas of fluid-based processing, turbine blade erosion, and reactor wall abrasion.

Key words: Wall contact effects; Computational fluid dynamics and discrete element method (CFD-DEM); Particle-wall collision; Two-phase particle fluid
http://dx.doi.org/10.1631/jzus.A1700039 **CLC number:** O35

1 Introduction

The two-phase particle fluid widely exists in many engineering areas, such as mechanical processing, fluid machinery, chemical reaction, processing equipment, metallurgy, and pipe transportation (Ku and Lin, 2008; Ji *et al*., 2012a; Tan and Zhang, 2014; Tan *et al*., 2016; Wang *et al*., 2016; Zhang *et al*., 2016; Jin *et al*., 2017). As a special fluid medium, it is commonly driven by a fluid power device and forms a flow state in a finite physical space (flow passage or vessel), in which the particle-wall collision occurs caused by the control effects of a two-phase flow field.

Related research suggests that the particle-wall collision is a complex liquid-solid coupling dynamic issue with highly nonlinear characteristics (Guala and Stocchino, 2007; Ren *et al*., 2011; Chen *et al*., 2013). Considering the inter-collisions of different particles, it can be regarded as a chaotically dynamic. Therefore, work that establishes the physical mechanism of the particle-wall collision process and reveals the motion laws of particles has scientific values and useful prospects for engineering.

Given the high complexity and nonlinear characteristics, modeling and solving for particle-wall collision processes are very difficult. The computational fluid dynamics (CFD) methods oriented to two-phase particle fluid can be classified into two

---

‡ Corresponding author

* Project supported by the National Natural Science Foundation of China (Nos. 51375446 and 51575494) and the Zhejiang Provincial Natural Science Foundation of China (Nos. LR16E050001 and LZ14E050001)

ORCID: Da-peng TAN, http://orcid.org/0000-0002-6018-9648

categories: Eulerian-Lagrangian method (ELM) and Eulerian-Eulerian method (EEM) (Tan *et al.*, 2010; 2013; 2015; Lopez *et al.*, 2015; Mansouri *et al.*, 2015). In the hypothesis of ELM, the particle is treated as a discrete element, and the individual motion of the particle can be obtained. Cao and Cheung (2014) presented an ELM-based particle flow modeling method, which regarded the water/air and particles as Eulerian phases and Lagrangian particles, respectively, and found the hydrodynamics condition and the trajectories of particles. Kowsari *et al.* (2016) adopted the volume-of-fluid (VOF) model which was used for the water-jet and the discrete phase model (DPM) to describe the motion laws of discrete particles, and derived a generalized relation between channel geometry and erosive flow. Nguyen *et al.* (2014) used the DPM to model particle flow in chemical mechanical polishing and then obtained the distribution of the particle concentration. With respect to the EEM, the solid phase is treated as a continuous phase to calculate the volume fraction. Wan *et al.* (2014) conducted CFD simulation to predict the surface roughness of abrasive flow machining. In their research, the particle medium was treated as a homogenous continuum with an average density, and the distribution laws of pressure and velocity along the workpiece were revealed. Ji *et al.* (2012b) used the mixture model and realizable k-ε turbulence model to analyze turbulent effects of particle flow in the near-wall region, and calculated turbulent energy under various particle concentrations in the flow passage.

For the above studies, the motion and distribution of discrete particles can be obtained based on related modeling-solving methods. Since the particles in DPM are assumed as mass points that do not have volume, it is impossible to calculate the motion process of the particle-wall collision. The EEM can perform the solution for the distribution of particles. However, the solid phase and fluid phase are all treated as continuous phases, so the accurate motion data of particle-wall collision motion cannot be ascertained. Moreover, previous work mainly focuses on the issues of particle trajectory and near-wall flow field, but the particle-wall collision mechanism and contact effects are unclear.

To address the above matters, we introduce the discrete element method (DEM) into the two-phase particle fluid area, and propose a coupled CFD-DEM modeling-solving method for the particle-wall collision process. The research process can be described as follows. (1) The flow field profiles are acquired by the CFD method as the initial motion conditions of solid particles. (2) The particles are regarded as ideal rigid bodies, and the motion laws are obtained by DEM. (3) The data interactions between CFD and DEM are derived by calculating interaction force and void fraction. (4) The accurate motion data including particle velocity, collision distribution, and collision force are obtained, and the mechanism of wall contact deformation and material removal can be revealed. (5) Particle image velocimetry (PIV) observation experiments are carried out to validate the effectiveness of the proposed method.

In general, the main scientific contribution of this paper is in providing a numerical computation method to examine the wall contact effects of two-phase particle fluid. This research can offer theoretical support to the modeling for a multi-phase particle fluid, and provide technical support for flow regulation of the areas of fluid-based precision processing, turbine blade cavitation erosion, and chemical reaction wall abrasion.

2 CFD-DEM coupled modeling method for particle-wall collision

As indicated in Section 1, the flowing state is two-phase particle flow in a limited physical space, which involves the following three mathematical models: the fluid governing equations, the particle motion equations, and the inter-phase coupling solution.

2.1 Governing equations for continuous fluid phase

The Euler multiphase flow model is widely used in multiphase research because it can well describe the interaction among different phases and the influence of the solid volume fraction. In the Euler model, the fluid phase and the particle phase are both treated as continuous phases, and there is mass transfer among different phases. In addition, the forces acting on the particle phase are calculated by means of the average parameters (local particle volume fraction, the velocity of particle phase, and fluid phase) (Ku and Lin, 2008; Ji *et al.*, 2012a; Tan and Zhang, 2014). However, in the CFD-DEM coupled method, the particles are modeled by means of DEM theory and are treated as the real discrete particles, so there is not mass transfer between the fluid phase and the particle phase, and the void fraction in each fluid grid cell is calculated by subtracting the volume of particles. Based on the Euler multiphase flow model, the governing equations for the continuous fluid phase are described as

$$\frac{\partial}{\partial t}(\alpha_{\mathrm{L}}\rho_{\mathrm{L}})+\nabla\cdot(\alpha_{\mathrm{L}}\rho_{\mathrm{L}}\boldsymbol{v}_{\mathrm{L}})=0, \tag{1}$$

$$\begin{aligned}&\frac{\partial}{\partial t}(\alpha_{\mathrm{L}}\rho_{\mathrm{L}}\boldsymbol{v}_{\mathrm{L}})+\nabla\cdot(\alpha_{\mathrm{L}}\rho_{\mathrm{L}}\boldsymbol{v}_{\mathrm{L}}\boldsymbol{v}_{\mathrm{L}})\\&\quad=-\alpha_{\mathrm{L}}\nabla\boldsymbol{p}+\nabla\cdot\bar{\bar{\tau}}_{\mathrm{L}}+\alpha_{\mathrm{L}}\rho_{\mathrm{L}}\boldsymbol{g}-\boldsymbol{S},\end{aligned} \tag{2}$$

where ρ_{L} and $\boldsymbol{v}_{\mathrm{L}}$ are the fluid density and velocity, respectively, α_{L} is void fraction in each fluid grid cell, $\boldsymbol{p}$ is the fluid pressure, $\boldsymbol{g}$ is the acceleration of gravity, and $\bar{\bar{\tau}}_{\mathrm{L}}$ is the stress-strain tensor of the fluid phase:

$$\bar{\bar{\tau}}_{\mathrm{L}}=\alpha_{\mathrm{L}}\eta_{\mathrm{L}}(\nabla\boldsymbol{v}_{\mathrm{L}}+\nabla\boldsymbol{v}_{\mathrm{L}}^{\mathrm{T}})+\alpha_{\mathrm{L}}(\lambda_{\mathrm{L}}-\frac{2}{3}\eta_{\mathrm{L}})\nabla\cdot\boldsymbol{v}_{\mathrm{L}}\bar{\bar{I}}, \tag{3}$$

where η_{L} and λ_{L} are the fluid shear viscosity and bulk viscosity, respectively, $\bar{\bar{I}}$ is the intensity of the turbulent kinetic energy, and $\boldsymbol{S}$ is the average force acting on the particles in each fluid grid cell:

$$\boldsymbol{S}=\frac{\sum_{i}^{m}\boldsymbol{F}_{\mathrm{D}}}{V_{\mathrm{L}}}, \tag{4}$$

where $\boldsymbol{F}_{\mathrm{D}}$ is the interaction force between particle and fluid, m is the number of particles in each fluid grid cell, and V_{L} is the volume of the fluid grid cell.

There is a large disturbance when various inlet fluids converge, and the Reynolds number has already exceeded the steady laminar flow Reynolds number. Thus, the turbulence model should be added to the governing equations:

$$\begin{aligned}&\frac{\partial}{\partial t}(\rho_{\mathrm{L}}k)+\nabla\cdot(\rho_{\mathrm{L}}\boldsymbol{v}_{\mathrm{L}}k)\\&\quad=\nabla\cdot\left(\left(\mu+\frac{\mu_{\mathrm{t}}}{\sigma_k}\right)\nabla k\right)+\boldsymbol{G}_k-\rho_{\mathrm{L}}\varepsilon,\end{aligned} \tag{5}$$

$$\begin{aligned}&\frac{\partial}{\partial t}(\rho_{\mathrm{L}}\varepsilon)+\nabla\cdot(\rho_{\mathrm{L}}\boldsymbol{v}_{\mathrm{L}}\varepsilon)\\&\quad=\nabla\cdot\left(\left(\mu+\frac{\mu_{\mathrm{t}}}{\sigma_\varepsilon}\right)\nabla\varepsilon\right)+C_1\boldsymbol{E}_{\mathrm{L}}\rho_{\mathrm{L}}\varepsilon-C_2\rho_{\mathrm{L}}\frac{\varepsilon^2}{k+\sqrt{v\varepsilon}},\end{aligned} \tag{6}$$

where μ is the fluid dynamic viscosity, k and ε are the turbulent kinetic energy and turbulent dissipation, v is motion viscosity coefficient, $\mu_{\mathrm{t}}=\rho_{\mathrm{L}}C_\mu\frac{k^2}{\varepsilon}$ is turbulent viscosity coefficient, C_μ is the function of the mean strain and rotation rates, σ_k=1.0 is the Prandtl number of the turbulent kinetic energy, σ_ε=1.2 is the Prandtl number of the turbulent kinetic energy dissipation rate, $\boldsymbol{G}_k=\mu_{\mathrm{t}}\left(\frac{\partial u_i}{\partial x_j}+\frac{\partial u_j}{\partial x_i}\right)\frac{\partial u_i}{\partial x_j}$ is the turbulent kinetic energy caused by the average velocity gradient, u_i and u_j are the velocity components, $C_1=\max\left(0.43,\frac{\boldsymbol{\eta}}{\boldsymbol{\eta}+5}\right)$, C_2=1.9 is an empirical value, and $\boldsymbol{\eta}=(2\boldsymbol{E}_{ij}\cdot\boldsymbol{E}_{ij})^{1/2}\frac{k}{\varepsilon}$. $\boldsymbol{E}_{ij}$ is the modulus of the time-averaged strain rate tensor and is calculated by $\frac{1}{2}\left(\frac{\partial u_i}{\partial x_j}+\frac{\partial u_j}{\partial x_i}\right)$, and $\boldsymbol{E}_{\mathrm{L}}=(2\boldsymbol{E}_{ij}\cdot\boldsymbol{E}_{ij})^{1/2}$.

Accordingly, the profiles of fluid pressure and velocity in flow passage can be obtained by solving the above equations, which are the initial motion conditions of the particles.

2.2 Discrete element method

DEM is a numerical analysis method for computing the structure and movement laws of non-continuous granular materials, and analyzing the contact force and motion of discrete particles (Kruggel-Emden *et al.*, 2007). In the framework of DEM, the motion of a particle is tracked in a Lagrangian way and is solved based on Newton's second law. Therefore, the motion equations of a discrete particle in liquid-solid two phase flow are formulated as

$$m_i\frac{\mathrm{d}\boldsymbol{v}_i}{\mathrm{d}t}=\boldsymbol{F}_{\mathrm{D}}+\boldsymbol{F}_{\mathrm{C}}+\boldsymbol{G}, \tag{7}$$

$$I_i \frac{\mathrm{d}\boldsymbol{\omega}_i}{\mathrm{d}t} = \boldsymbol{T}_i, \tag{8}$$

where t is time, $\boldsymbol{F}_\mathrm{C}$ and $\boldsymbol{G}$ are the collision force and gravity, m_i and $\boldsymbol{v}_i$ are the mass and velocity of particle i, I_i, $\boldsymbol{\omega}_i$, and $\boldsymbol{T}_i$ are the rotary inertia, angular velocity, and torque of particle i, respectively, and $\boldsymbol{F}_\mathrm{D}$ is the interaction force between fluid and particle:

$$\boldsymbol{F}_\mathrm{D}=\boldsymbol{F}_\mathrm{DRAG}+\boldsymbol{F}_\mathrm{P}+\boldsymbol{F}_\mathrm{B}+\boldsymbol{F}_\mathrm{VR}+\boldsymbol{F}_\mathrm{BT}+\boldsymbol{F}_\mathrm{SAFF}+\boldsymbol{F}_\mathrm{MAG}, \tag{9}$$

where $\boldsymbol{F}_\mathrm{DRAG}$, $\boldsymbol{F}_\mathrm{P}$, $\boldsymbol{F}_\mathrm{B}$, $\boldsymbol{F}_\mathrm{VR}$, $\boldsymbol{F}_\mathrm{BT}$, $\boldsymbol{F}_\mathrm{SAFF}$, and $\boldsymbol{F}_\mathrm{MAG}$ represent drag force, pressure gradient force, buoyant force, virtual mass force, Basset force, Saffman lift force, and Magnus force, respectively. When a pressure gradient is created in a flow field, the particle motion will be affected by the pressure gradient force (Gao *et al.*, 2002). The virtual mass force and Basset force should be considered if the solid density is similar to the fluid density (Li, 2012). The Saffman lift force and Magnus force are mainly caused by the fluid velocity gradient (Hu, 2010). In the application of this study, the variations of pressure gradient and velocity gradient will become extremely intense when the particles flow from non-constrained space into constrained flow passage (the structure of flow passage is shown in Fig. 5). Therefore, the pressure gradient force, Saffman lift force, and Magnus force need to be considered. Because the solid density is much higher than the liquid density, the virtual mass force and the Basset force can be ignored.

The drag force plays a major role in the forces acting on a particle. In the flow process of a particle fluid, there are high particle concentration regions. Therefore, the drag force equation which considers the impact of the void fraction is adopted (Kotrocz *et al.*, 2016):

$$\boldsymbol{F}_\mathrm{DRAG} = \frac{C_\mathrm{D}}{8}\pi d_\mathrm{P}^2 \rho_\mathrm{P} \left|\boldsymbol{v}_\mathrm{L} - \boldsymbol{v}_\mathrm{P}\right| \left(\boldsymbol{v}_\mathrm{L} - \boldsymbol{v}_\mathrm{P}\right) \alpha_\mathrm{L}{}^{-(\chi+1)}, \tag{10}$$

$$\chi = 3.7 - 0.65\exp\left[-(1.5 - \log Re_\mathrm{P})^2/2\right], \tag{11}$$

where ρ_P, $\boldsymbol{v}_\mathrm{P}$, and d_P are the density, velocity, and diameter of particle, respectively. C_D and Re_P are the drag coefficient and Reynolds number of particle, and are calculated by

$$C_\mathrm{D} = \left(0.63 + \frac{4.8}{Re_\mathrm{P}^{0.5}}\right)^2, \tag{12}$$

$$Re_\mathrm{P} = \frac{\alpha_\mathrm{L}\rho_\mathrm{P} d_\mathrm{P}\left|\boldsymbol{v}_\mathrm{L} - \boldsymbol{v}_\mathrm{P}\right|}{\mu_\mathrm{L}}, \tag{13}$$

where μ_L is the dynamic viscosity coefficient of the fluid.

For the contact effects of particle-wall collision, it is necessary to obtain the collision force. Fig. 1 shows a contact process between the particles i and j (j stands for particle j or wall j), in which $\boldsymbol{\alpha}$ is the normal displacement and $\boldsymbol{\delta}$ is the tangential displacement. The soft sphere model is adopted to calculate the collision force. This model mainly uses an elastic coefficient and a damping coefficient to simplify the contact process, and assumes that parameters stay the same in the contact process. The particle-wall contact process can be described by the soft sphere model, as shown in Fig. 2.

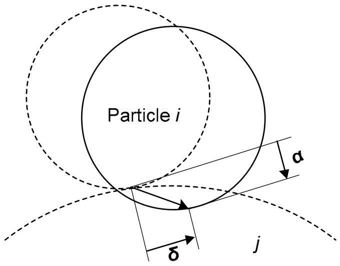

Fig. 1 Schematic diagram of particle-wall contact process

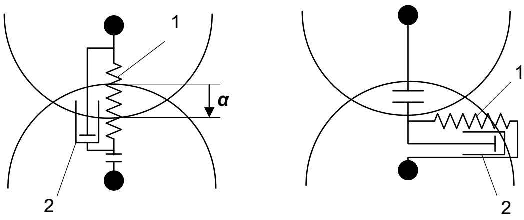

(a) (b)

Fig. 2 Soft sphere based particle-wall contact model
(a) Normal contact; (b) Tangential contact. 1: spring; 2: damper

It can be seen in Fig. 2 that the soft sphere model sets springs and dampers between particles i and j. The collision force can be decomposed into a normal collision force and a tangential collision force, and the normal collision force is

$$\boldsymbol{F}_{\mathrm{N}ij}=(-k_{\mathrm{N}}\boldsymbol{\alpha}^{3/2}-\eta_{\mathrm{N}}\boldsymbol{G}_{\mathrm{R}}\boldsymbol{n})\boldsymbol{n}, \tag{14}$$

where $\boldsymbol{G}_{\mathrm{R}}$ is the relative velocity between particles i and j, $\boldsymbol{n}$ is unit vector from the sphere center of particle i to j, and k_{N} and η_{N} are the normal elastic coefficient and normal damping coefficient of particle i, respectively, and are defined by

$$k_{\mathrm{N}}=\frac{4}{3}\left(\frac{1-\upsilon_i^2}{E_i}+\frac{1-\upsilon_j^2}{E_j}\right)^{-1}\left(\frac{a_i+a_j}{a_ia_j}\right)^{-1/2}, \tag{15}$$

$$\eta_{\mathrm{N}}=2\sqrt{m_{\mathrm{P}}k_{\mathrm{N}}}, \tag{16}$$

where E_i and E_j are the elastic moduli of particles i and j, υ_i and υ_j are Poisson's ratios of particles i and j, a_i and a_j are the radii of particles i and j, respectively, and m_{P} is the mass of particle. Similar to the normal collision force, the tangential collision force is expressed as

$$\boldsymbol{F}_{\mathrm{T}ij}=-k_{\mathrm{T}}\boldsymbol{\delta}-\eta_{\mathrm{T}}\boldsymbol{G}_{\mathrm{T}}, \tag{17}$$

where k_{T} and η_{T} are the tangential elastic coefficient and tangential damping coefficient, and are given by

$$k_{\mathrm{T}}=8\boldsymbol{\alpha}^{1/2}\left(\frac{1-\upsilon_i^2}{\boldsymbol{G}_i}+\frac{1-\upsilon_j^2}{\boldsymbol{G}_j}\right)^{-1}\left(\frac{a_i+a_j}{a_ia_j}\right)^{-1/2}, \tag{18}$$

$$\eta_{\mathrm{T}}=2\sqrt{m_{\mathrm{P}}k_{\mathrm{T}}}. \tag{19}$$

$\boldsymbol{G}_{\mathrm{T}}$ is the slip velocity in the contact point:

$$\boldsymbol{G}_{\mathrm{T}}=\boldsymbol{G}-(\boldsymbol{G}\boldsymbol{n})\boldsymbol{n}+a_i\boldsymbol{\Omega}_i\times\boldsymbol{n}+a_j\boldsymbol{\Omega}_j\times\boldsymbol{n}, \tag{20}$$

where $\boldsymbol{\Omega}_i$ and $\boldsymbol{\Omega}_j$ are the angular velocities of particles i and j, respectively. Thus, the collision force and torque acting on particle i are respectively expressed as

$$\boldsymbol{F}_{ij}=\boldsymbol{F}_{\mathrm{N}ij}+\boldsymbol{F}_{\mathrm{T}ij}, \tag{21}$$

$$\boldsymbol{T}_{ij}=a_i\boldsymbol{n}\times\boldsymbol{F}_{\mathrm{T}ij}. \tag{22}$$

In liquid-solid two phase flow, a lot of particles may be in contact at the same time. Therefore, the total collision force and torque acting on particle i are given by

$$\boldsymbol{F}_{\mathrm{C}}=\sum_{j=1}^{m}(\boldsymbol{F}_{\mathrm{N}ij}+\boldsymbol{F}_{\mathrm{T}ij}), \tag{23}$$

$$\boldsymbol{T}_{\mathrm{C}}=\sum_{j=1}^{m}(a_i\boldsymbol{n}\times\boldsymbol{F}_{\mathrm{T}ij}). \tag{24}$$

In the particle-wall collision process, there will be a great change in speed and pressure when the particles flow from the non-constrained to the constrained space flow field. Therefore, the pressure gradient force, Saffman lift force, and Magnus force must be considered, and can be calculated by

$$\boldsymbol{F}_{\mathrm{P}}=-\frac{1}{6}\pi d_{\mathrm{P}}^3\frac{\mathrm{d}\boldsymbol{p}}{\mathrm{d}x}, \tag{25}$$

$$\boldsymbol{F}_{\mathrm{SAFF}}=1.615d_{\mathrm{P}}^2\sqrt{\rho_{\mathrm{L}}\mu_{\mathrm{L}}}(\boldsymbol{v}_{\mathrm{L}}-\boldsymbol{v}_{\mathrm{P}})\sqrt{\left|\frac{\mathrm{d}\boldsymbol{v}_{\mathrm{L}}}{\mathrm{d}y}\right|}, \tag{26}$$

$$\boldsymbol{F}_{\mathrm{MAG}}=\frac{\pi}{8}d_{\mathrm{P}}^3\rho_{\mathrm{L}}(\omega\times(\boldsymbol{v}_{\mathrm{P}}-\boldsymbol{v}_{\mathrm{L}}))\left[1+\theta(R)\right], \tag{27}$$

where $\theta(R)$ is a remainder, and its order of magnitude is much more smaller than other items. R is the remainder expansion point. Buoyant force and gravity can also be defined respectively as

$$\boldsymbol{F}_{\mathrm{B}}=\rho_{\mathrm{L}}\boldsymbol{g}V_{\mathrm{P}}, \tag{28}$$

$$\boldsymbol{G}=m_{\mathrm{P}}\boldsymbol{g}, \tag{29}$$

where V_{p} is the volume of the particle.

The particles are treated as ideal rigid bodies, and the accurate motion trajectories of particles can be calculated by DEM theory. In combination with the soft sphere model, the motion laws and dynamic characteristics of the particle-wall collision process can be obtained.

2.3 An inter-phase coupling solution method

The data interactions between CFD and DEM are implemented by calculating the forces ($\boldsymbol{F}_{\mathrm{DRAG}}$, $\boldsymbol{F}_{\mathrm{P}}$, $\boldsymbol{F}_{\mathrm{B}}$, $\boldsymbol{F}_{\mathrm{SAFF}}$, and $\boldsymbol{F}_{\mathrm{MAG}}$) and the fluid void fraction (α_{L}). By calculating the particles' volume fraction (α_{P}), we can obtain the fluid void fraction.

As shown in Fig. 3, every particle in the fluid grid cell is surrounded by a bounding box, and then we count the sample points in the bounding box. If the sample points locate in the particle and fluid grid cell, they will be saved. Therefore, the particle volume fraction in a fluid grid cell can be obtained by

$$\alpha_{\mathrm{P}} = 1 - \alpha_{\mathrm{L}} = \frac{n_{\mathrm{C}}}{N} V_{\mathrm{P}}, \tag{30}$$

where n_{C} is the sum of sample points located in the particle and fluid grid cell, and N is the sum of the sample points which are located in a bounding box.

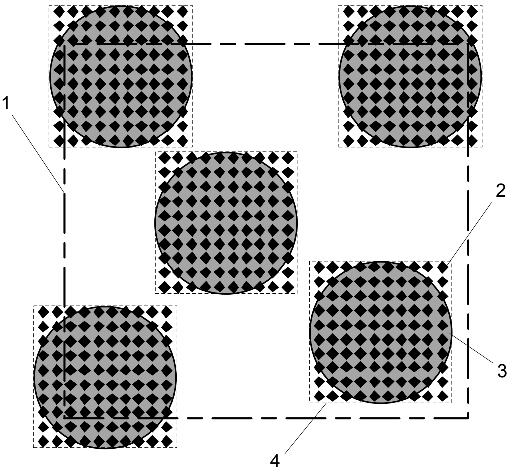

Fig. 3 Sample points of particles within the fluid grid cell
1: fluid grid cell; 2: sample point; 3: particle; 4: bounding box

Based on the above hypothesis, an inter-phase coupling solution method for particle-wall collision is proposed, and the procedures are shown in Fig. 4. First, the continuous fluid phase is discretized with fluid grid cells, and the governing equations are solved by CFD methods. Then, if a stable solution is obtained, the coupling module begins to calculate the related velocities between the fluid and the particles, and calculate the interaction forces ($\boldsymbol{F}_{\mathrm{D}}$). Subsequently, the interaction forces are then inputted to the DEM framework, and the particles' motion trajectories are calculated. At the same time, the contact equations will be activated if there are particles in the contacting states. Finally, the velocities and the positions of the particles are updated. After one CFD time step, the new positions of particles will be input back into the CFD grid cells, and the void fraction α_{L} is updated, and then the CFD solver begins a new round of iterative calculation.

Owing to the randomness of the particle-wall (particle-particle) collision process, the two-phase particle fluid in the above CFD-DEM coupled solution process is a kind of non-steady fluid. By the above coupling solution method, the positions of all particles are continuously updated, the particle motion trajectories can be acquired, and the related dynamic parameters involved by the particle-wall contact effects can be obtained.

3 Physical model and boundary conditions

We take fluid-based precision processing (FPP), which uses the particle-wall collision to process the surface of the workpiece, as an instance to illustrate the corresponding research.

3.1 Physical objective

The working principle of FPP is shown in Fig. 5. There are three abrasive particle flow inlets around the circumference of the processing tool, and the angle of any two inlets is 120°, as shown in Fig. 5b. Under the drive of the pumps, the particle flow first enters the non-constrained space along inlets at a high flow velocity, and then flows into the constrained space between the workpiece and processing tool. Owing to the decrease of flow passage scale, the

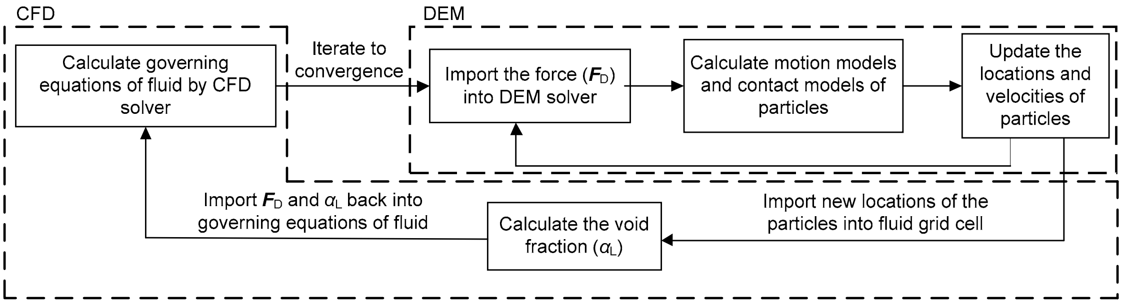

Fig. 4 Inter-phase coupling solution method for particle-wall collision

particle flow is accelerated to a higher flow velocity. Fig. 5c is an enlarged view of the constrained space. The bottom surface of the processing tool is designed as an inclined plane to guarantee high flow velocity along the workpiece. The workpiece is processed through the continuous wall contact effects of the particle-wall collision process.

3.2 Boundary conditions

According to the FPP working principle illustrated in Fig. 5, a geometrical model of the constrained flow passage is set up, as shown in Fig. 6, where the diameter of the inlet (*D*) is a key parameter of the fluid dynamic system, and the bottom surface of the constrained flow passage is the surface of the workpiece.

During the course of employing a CFD-DEM coupled solution, to ensure the stability of solution and the continuity of flow field, the size of particle should be smaller than that of the calculation grid. At the same time, the size of calculation grid should promise the solution accuracy of flow field. For the geometrical model, a grid model with 71 857 tetrahedral mesh cells is built up, as shown in Fig. 7. Then, the boundary conditions are confirmed, and the grid independence validation is performed. Subsequently, the semi-implicit method for pressure-linked equations (SIMPLE) algorithm is adopted to deal with the pressure-velocity coupling and pressure discrete interpolation. A finite volume method based on first-order upwind scheme is adopted to discretize the momentum, turbulent kinetic energy, and turbulent dissipation rate.

The volume fraction of particles is in the range of 10%–15%, and we guarantee the volume fraction by defining birth rate in the simulation process. The restitution coefficient of the particle-wall collision should be obtained through experimental measurement, but mostly particle-wall collisions are elastic collisions. In this study, we adopted the restitution coefficient verified by Kuwagi (Sun and Wang, 2009), and the other physical parameters are listed in Table 1. To reduce the overall computer run time, the simulations are carried out using the parallel versions

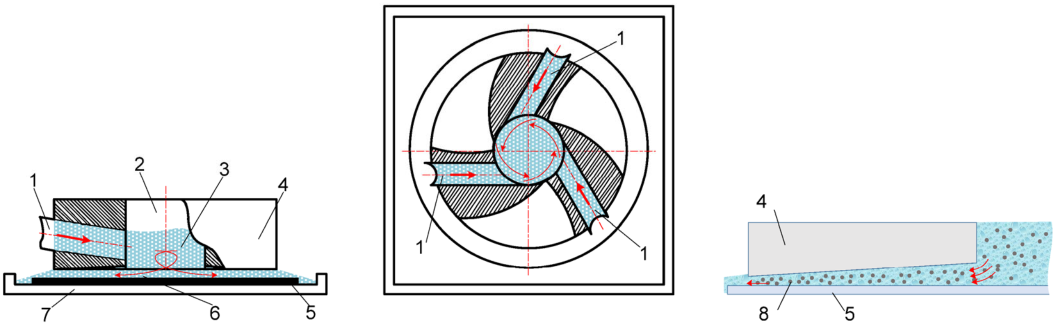

(a) (b) (c)

Fig. 5 Abridged view of physical objective

(a) Orthogonal view of FPP tool; (b) Vertical view of FPP tool (a vortex flow file is formed by the three inlets); (c) Constrained physical space structure. 1: inlet; 2: non-constrained space; 3: abrasive flow; 4: processing tool; 5: workpiece; 6: constrained flow passage; 7: fixture; 8: abrasive particle

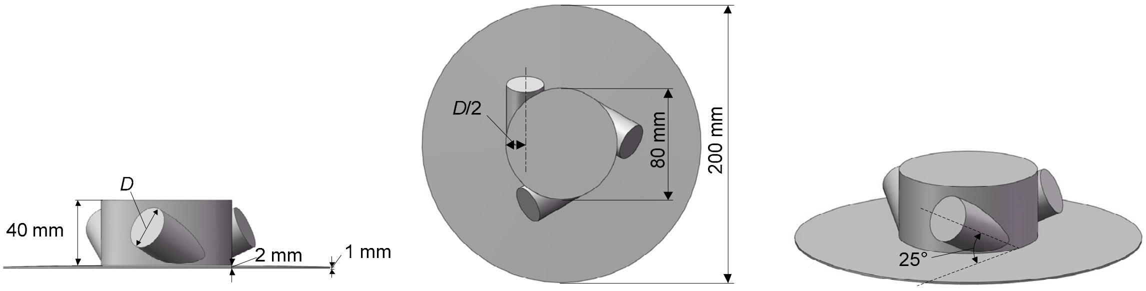

(a) (b) (c)

Fig. 6 Geometrical model of constrained flow passage

(a) Orthogonal view; (b) Vertical view; (c) Axis view (the injection angle of inlet is 25°)

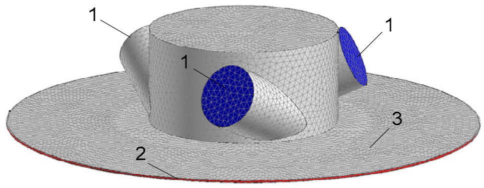

Fig. 7 Mesh generation and boundary conditions
1-velocity inlet, 2-outflow, 3-wall

Table 1 Physical parameters for numerical computation

Parameter	Value
Inlet velocity of fluid, $\boldsymbol{v}_{\rm L}$ (m/s)	22
Fluid density, $\rho_{\rm L}$ (kg/m^3)	900
Particle density, $\rho_{\rm P}$ (Kg/m^3)	3200
Particle diameter, $d_{\rm P}$ (μm)	100
Number of particles, $P_{\rm N}$	2×10^5
Shear modulus of particles, Q (Pa)	1×10^8
Poisson's ratio of particles, υ	0.25
Restitution coefficient, e	0.9
Static friction coefficient, $\mu_{\rm S}$	0.15
Rolling friction coefficient, $\mu_{\rm R}$	0.01
Time step of CFD, $\Delta t_{\rm CFD}$ (s)	1.21×10^{-5}
Time step of DEM, $\Delta t_{\rm DEM}$ (s)	2.42×10^{-7}

of the fluent solver and the engineering discrete element method (EDEM) solver.

4 Results and discussion

By the above models and inter-phase coupling solution method, the numerical simulations for the particle-wall collision process are performed, and the results are indicated and discussed as follows.

The convergence of the inter-phase coupling solution has three criteria: the difference of inlet and outlet mass flow rates is less than 0.1%; the physical value of monitoring point does not change as the iteration increases; the macroscopic particle distribution remains stable as the particles are injected. The difference of inlet and outlet mass flow rates is about 0.0015%; Fig. 8 shows the fluid velocity variation of the monitoring point when the fluid dynamic viscosity is μ=0.005 kg/(m·s), and it can be seen that the fluid velocity has remained stable as the iteration increases; the macroscopic particle distribution also has reached a stable state as shown in Fig. 9f.

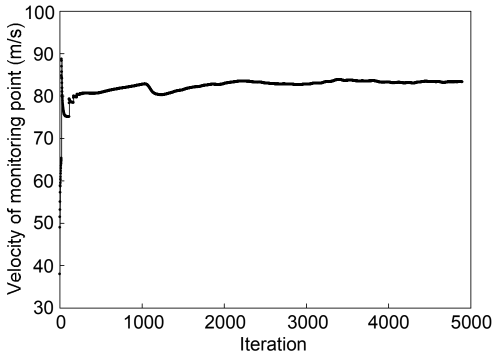

Fig. 8 Velocity variation of monitoring point (D=20 mm, μ=0.005 kg/(m·s))

4.1 Contacting state description

The physical calculation domain of particle flow, which matches the flow passage, is selected by the rectangular box as shown in Fig. 10a. The particle motion processes in the rectangular box will be all calculated, and the 3D velocity profile of particle flow can be obtained.

It can be seen from the partially enlarged view (Fig. 10b) that a lot of particles collide with each other continuously under the driving of the fluid medium, and particles impact the wall at different angles and velocities. Owing to a frequent collision approximating to chaotic state, the particle velocity distributions may also be different within a small region of fluid.

4.2 Macroscopic flow field profiles

The macroscopic flow field can reflect the collective motion laws of particles. The six time points from start injection to full-mixing of particle fluid are selected as the observation points, and the results for macroscopic velocity are shown in Fig. 9. From the figure, it can be inferred that the particles are accelerated as soon as they enter the flowing passage. At the center of the flowing passage, the particles from three different inlets converge and collide with the wall, as shown in Figs. 9c–9e. Under the acceleration effects of the swirling flow field, the particles flow into the constrained passage with higher velocities.

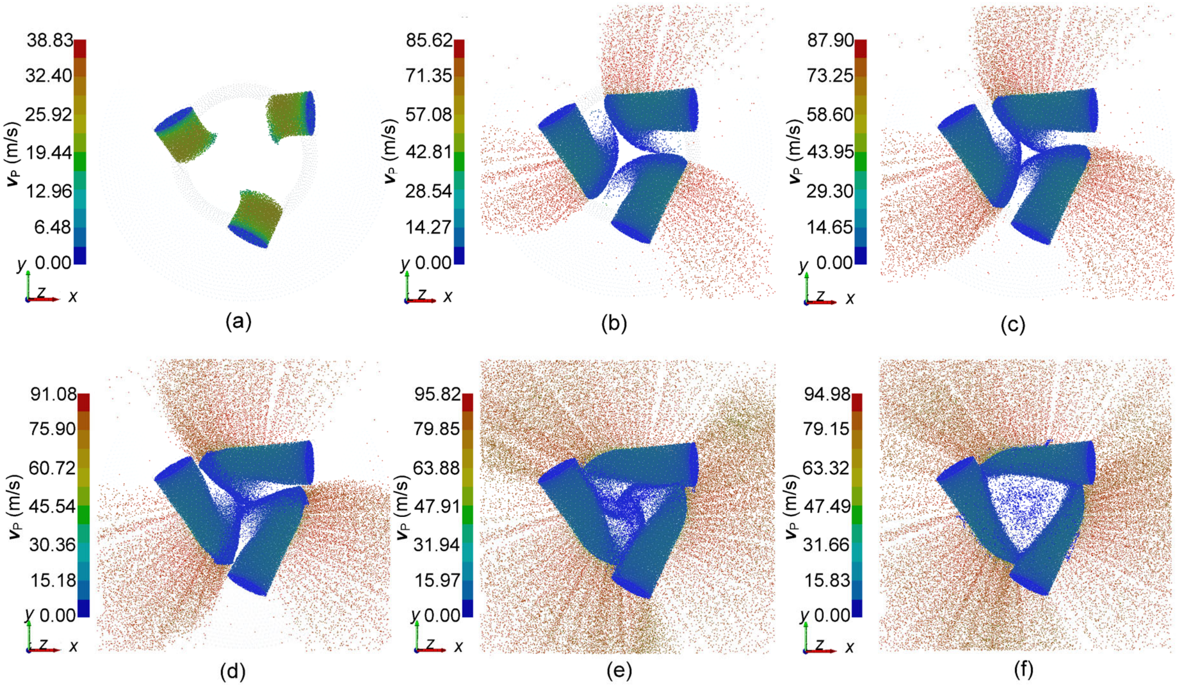

Fig. 9 Macroscopic velocity profiles of particles (D=20 mm, μ=0.005 kg/(m·s))

(a) t=0.001 s; (b) t=0.003 s; (c) t=0.0037 s; (d) t=0.0045 s; (e) t=0.0065 s; (f) t=0.01 s

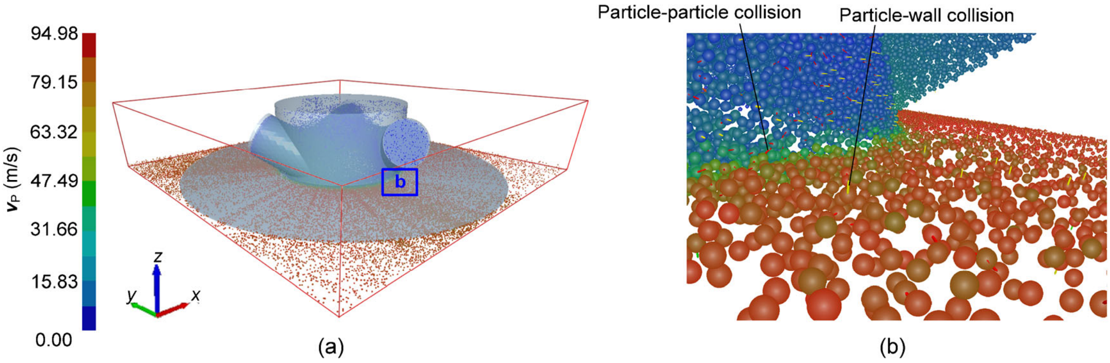

Fig. 10 Axis view of macroscopic particle fluid (D=20 mm, μ=0.005 kg/(m·s), t=0.01 s)

(a) Global view; (b) Partially enlarged view of region b

For the periphery flow field, there are radial texture phenomena on the profiles of particle motion trajectories (Figs. 9b–9e), which are caused by the flowing interference of the particle fluid. Accordingly, the motion interference will lead to uneven profiles of flow field in the constrained passage.

Apparently, the particle flow can form a relatively stable motion state in a short time. As shown in Fig. 9e, the particles' velocities in the center region have arrived at the maximum amplitude. Then, the center region forms a stable vortex flow field, and the velocities tend to decrease, as shown in Fig. 9f. For the fluid velocity profile on the wall (Fig. 11), there are apparent cycle-shape regions; the central region has the lowest velocity, and it can be regarded as a rigid core of a Rankine vortex.

For the low-speed region, the wall contact effects of particles tend to be limited because of their lower kinetic energy. We can also see that the particle distribution is not as uniform as the fluid in constrained space. More details are given in the following sub-sections.

4.3 Contact effects in relation to inlet diameters

It is well known that the flow passage structure has significant effects on the flow field, and thus it will affect the motion laws and dynamic characteristics of the particle-wall collision process. As indicated in Section 3, the diameter of the inlet is a key parameter of this fluid dynamic system. Thus, three numerical cases with different inlet diameters are provided, and the parameters are listed in Table 2.

Since the contact point positions of particles in the collision process can characterize the wall contact effects, the results of contact positions on the wall are obtained, as shown in Figs. 12a–12c. Then, to analyze the motion interference phenomena affected by passage inlets, we rotate the inlets 60°, and make the contact results overlay the results of no rotation, as shown in Figs. 12d–12f.

The inlets being rotated, the uniformities of contact point distributions apparently improve. In Fig. 12d, the blank areas still exist, especially for the central region of flow field, which illustrates the fact that the rotating motion of the vortex core can make

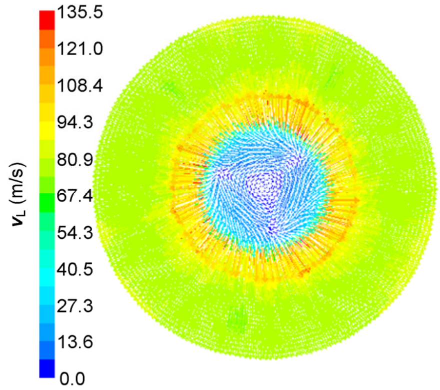

Fig. 11 Fluid velocity profile on the wall (D=20 mm, μ=0.005 kg/(m·s), t=0.01 s)

Table 2 Parameters of cases with different inlet diameters

Case	Inlet diameter, D (mm)	Fluid dynamic viscosity, μ (kg/(m·s))
a	13	0.005
b	20	0.005
c	27	0.005

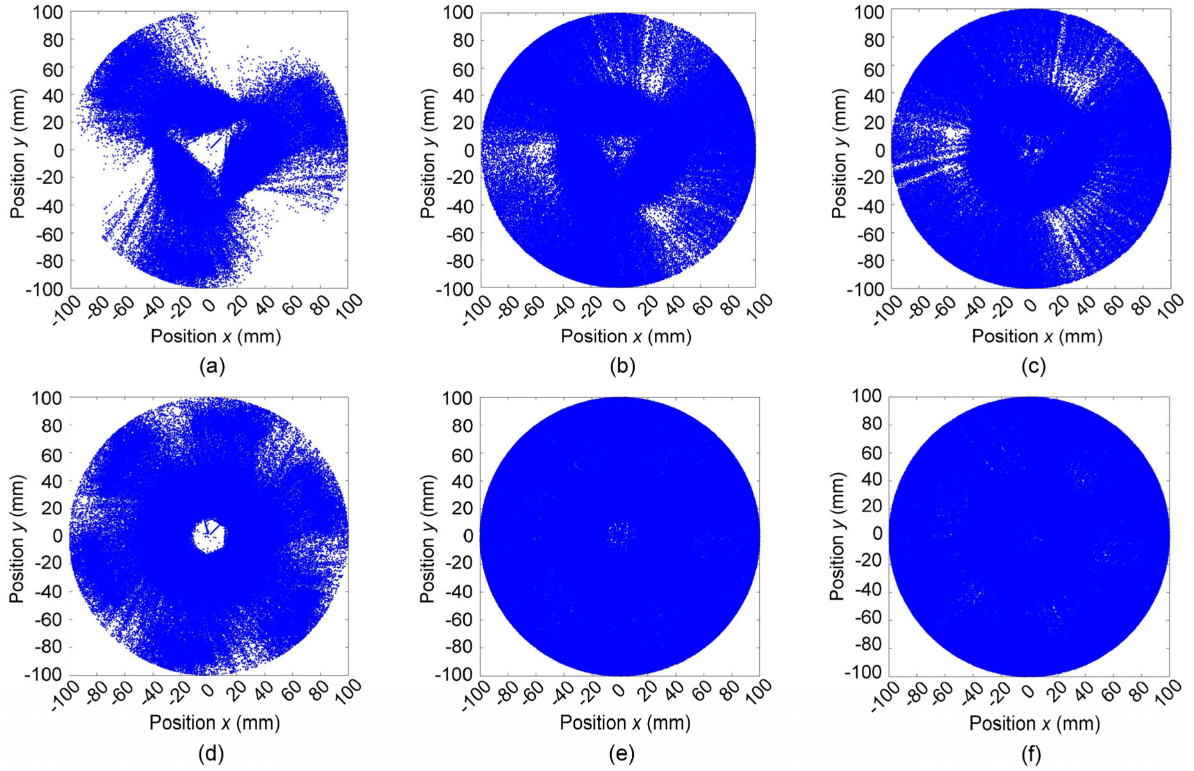

(a) (b) (c) (d) (e) (f)

Fig. 12 Contact point distributions for different inlet diameters (t=0.01 s)

(a) No rotation, D=13 mm; (b) No rotation, D=20 mm; (c) No rotation, D=27 mm; (d) Rotation overlapped, D=13 mm; (e) Rotation overlapped, D=20 mm; (f) Rotation overlapped, D=27 mm the contact probabilities decline. In Figs. 12e and 12f, there are no obvious blank areas; when *D*=20 mm, the contact distribution with rotating superposition can reach its best uniformity.

4.4 Contact effects in relation to viscosity

4.4.1 Contact point distributions

Viscosity is a key parameter of fluid motion, especially for turbulent flow. Six numerical cases with different viscosities are provided, and the physical parameters are listed in Table 3. Similarly, the results of contact point distributions for different viscosities are obtained, as shown in Fig. 13.

From the figures, we can find the laws as follows. (a) As the increment of viscosity is incrementally increased, the contact probabilities of the central region of the flow field tend to decline, and there is an obvious blank area in Fig. 13c. The results prove that the higher viscosity can make the vortex intensity decrease. (b) For the constrained flow passage, the contact distributions decrease and become sparser with the increment of viscosity (Figs. 13d–13f). This indicates that the turbulent motion state of particles is weakened with the increase of viscosity. As a result, the particle-wall collision frequency decreases, and the trajectories of particles are more consistent with the macroscopic flowing of fluid.

To further illustrate the above viewpoint, the particles that are transported out of the flow passage in a certain time segment (2 s) are counted. At the same time, the fluid velocities which locate in the outlet of flow passage are calculated, and the results are shown in Fig. 14. It can be seen that the number of particles increases with the increase of viscosity. By contrast, the fluid velocity decreases. Apparently, the higher viscosity can carry more particles, and the transporting ability of the fluid medium is improved. The above results reveal that the viscous forces acting

Table 3 Parameters of cases with different inlet viscosities

Case	Fluid dynamic viscosity, μ (kg/(m·s))	Inlet diameter, D ($\times10^{-3}$ m)
a	0.005	20
b	0.03	20
c	0.06	20
d	0.09	20
e	0.12	20
f	0.15	20

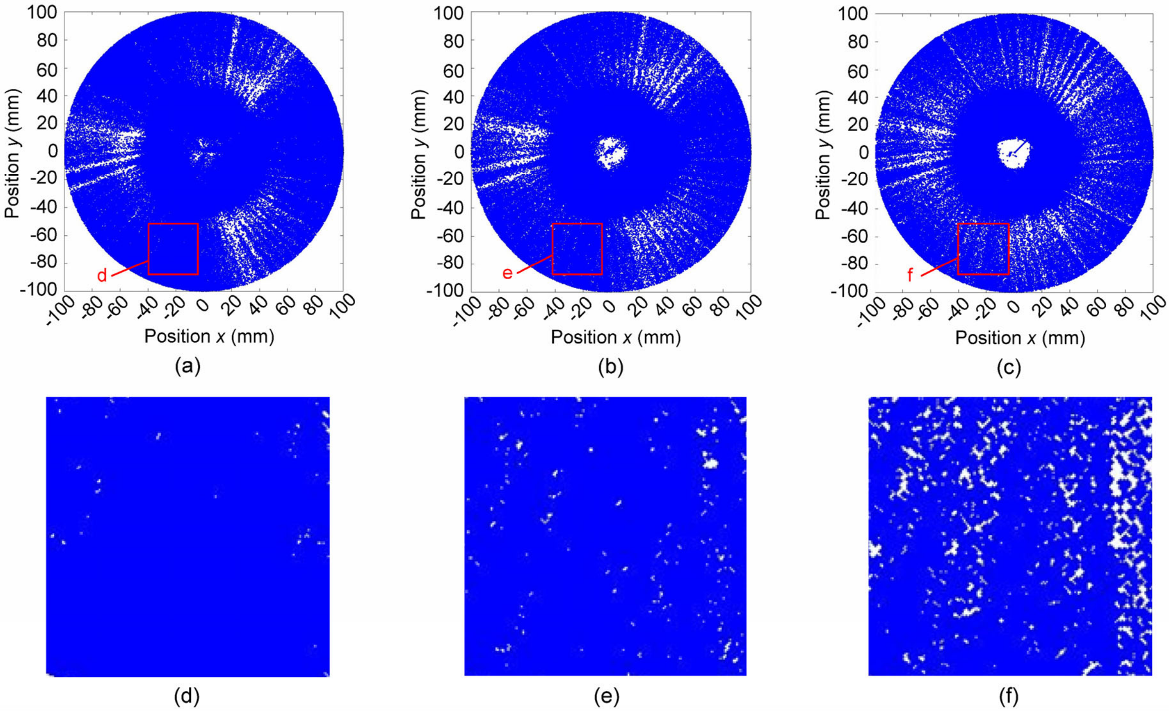

Fig. 13 Contact point distributions with different viscosities (*t*=0.01 s)

(a) Global view, μ=0.005 kg/(m·s); (b) Global view, μ=0.03 kg/(m·s); (c) Global view, μ=0.06 kg/(m·s); (d) Partially enlarged view of (a); (e) Partially enlarged view of (b); (f) Partially enlarged view of (c) on the particles are more remarkable with the increase of viscosity, and thereby the particle motion becomes more stable. This result accords with that shown in Fig. 13.

From the principles of fluid mechanics, the change of viscous force, which acts on the particles, will lead to variations of particle-wall collision velocity and collision pressure. Accordingly, the next sub-sections mainly concentrate on these two variables.

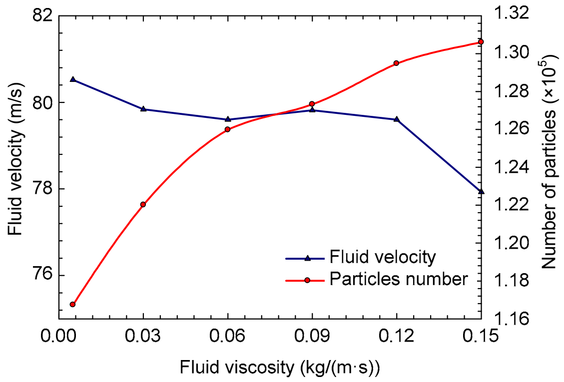

Fig. 14 Variations of fluid velocity and number of particles with fluid viscosity

4.4.2 Collision velocity distributions

In order to analyze the variations of particle-wall collision velocities and particle-wall collision pressures with viscosity, 14 sample points on the wall are selected, as shown in Fig. 15. The sample points are circular areas with a diameter of 2 mm. It can be seen from Fig. 12 that the uniform collision distribution mainly appears 120° apart, and the contact uniformity can be achieved by rotating the passage inlets. Therefore, we mainly study the particle-wall collision velocities and collision pressures which locate in the uniform collision distribution.

The collision velocities of sample points are extracted, and the results are shown in Fig. 16. It can be seen from Fig. 15 that the region between 0–0.04 m is non-constrained space, and the region between 0.04–0.1 m is constrained space. Since the wall in non-constrained space is affected mainly by the oblique impact of particles, the collision velocities take on a linearly increasing trend. Owing to the control effects of the constrained passage, the collision velocities increase rapidly as soon as the particles enter the constrained space. With the increase of viscosity, the accelerating effect becomes more apparent. By the increment of viscous resistance between the fluid and wall in constrained space, the collision velocities at the high viscosity decrease rapidly and finally reach stable motion states.

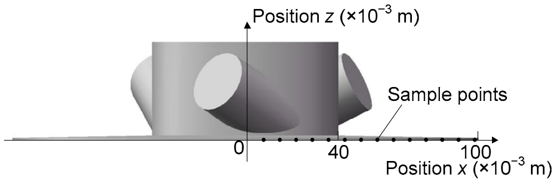

Fig. 15 Sample points on the wall

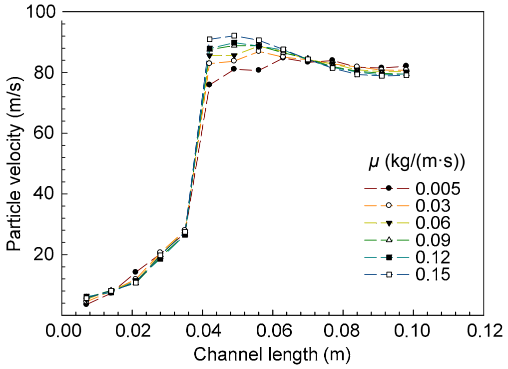

Fig. 16 Particle velocity distributions on the wall for six fluid viscosities

4.4.3 Collision pressure distributions

In the stable motion period, the particle-wall contact forces which locate in a sample point are summed together, and the particle-wall collision pressure in this sample area can be calculated. In this way, the collision pressures in different sample areas can be obtained, as shown in Fig. 17.

From the figure, the following observations can be made. (a) The particle-wall collision pressures increase initially and then decrease sharply to a stable state. (b) From the macroscopic particle flow field (Fig. 9) we can find that the maximum collision pressure is caused by the oblique impact when particles enter the flow passage, and increases with the incremental increase of fluid viscosity. (c) The collision pressures of the other sample points are mainly actuated by fluid turbulent motion, and decrease with the incremental increase of fluid viscosity.

The above results illustrate that the particle-wall collision pressure and collision velocity are affected

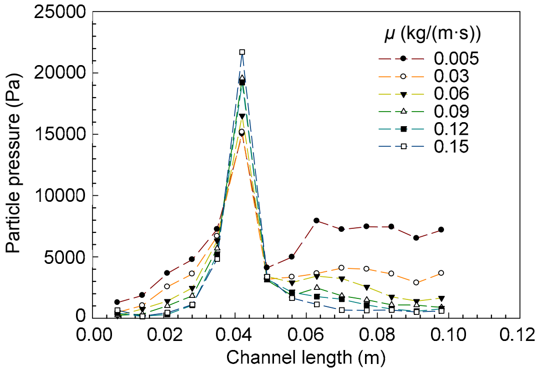

Fig. 17 Particle-wall collision pressure distributions on the wall

by synthetic actions of motion modes of fluid in the near-wall region and fluid viscosity: in the case of impact flowing, the particle-wall collision pressure and collision velocity increase with the increase of fluid viscosity because of the drag action; if the fluid flow direction is parallel to the wall, the particle-wall collision pressure and collision velocity mainly depend on the turbulent motion of the fluid, and decrease with the increase of fluid viscosity.

4.4.4 Material removal

Material removal is of considerable significance for the engineering areas of fluid-based precision processing, turbine blade cavitation erosion, and chemical reaction wall abrasion, and commonly described by the Preston equation. Here, the dimensionless material removal rate R^+ is defined as

$$R^+ = Z/K_\mathrm{P} = \boldsymbol{v} \cdot \boldsymbol{p}, \tag{31}$$

where Z is the material removal rate, the Preston constant K_P is obtained by experimental testing, and Z/K_P can be treated as the measurement of material removal rate. Using the equation, the dimensionless material removal rates for six viscosities are obtained, as shown in Fig. 18.

It can be seen from Fig. 18 that the material removal rate is not uniform along the radial direction of the wall, and has the following characteristics. (a) There is a lower material removal rate in the center region of the wall. The material removal rate reaches a maximum in the region where the particles enter the initial constrained space, and then the material removal rate decreases sharply. Therefore, in order to obtain uniform surface quality, the flow passage should not only intermittently rotate, but also should translate in the horizontal and vertical. (b) The viscosity has a large impact on the material removal rate. With the increase of viscosity, the material removal rate in non-constrained space and in initial constrained space increases, but in constrained space decreases. It can be seen that the removal rate difference between the maximum and minimum reduces with the decrease of viscosity. The above results indicate that contact uniformity can be more easily achieved by the low viscosity fluid.

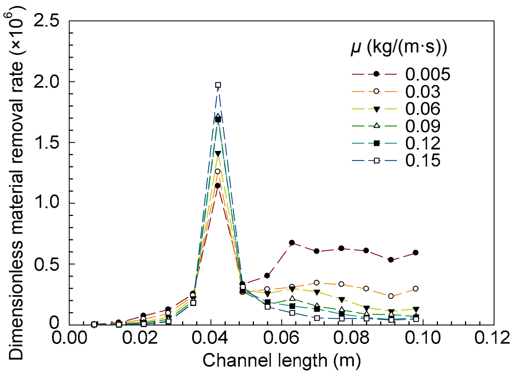

Fig. 18 Distributions of material removal rate for six viscosities

5 PIV validation experiments

PIV is an effective observation technique in experimental fluid mechanics (Wu *et al.*, 2013). By tracking the displacement of tracer particles, the instantaneous velocity vector field can be acquired. To verify the proposed modeling method, a physical objective model which is made of acrylic material is developed (Fig. 19a), and the PIV observation experiments are performed. PIV boundary conditions are consistent with simulation boundary parameters. The fluid medium is water. The parameters of the PIV apparatus are as follows: trigger rate is 7 Hz, time between pulses is 400 μs, and one-time acquisition includes 200 images.

Figs. 19b and 19c give the average velocity vector profile on the wall. It can be seen that the velocity vector field can be divided into two regions: A and B. The A region has the lowest velocity, and can be regarded as a rigid core of Rankine vortex. This is

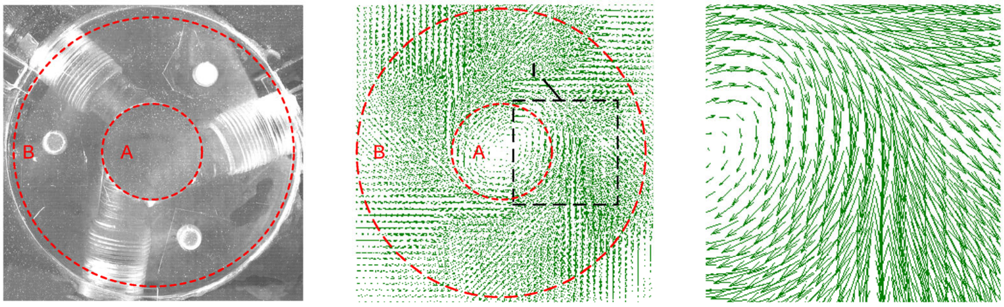

(a) (b) (c)

Fig. 19 PIV observation experiments

(a) Observation flow passage; (b) Average velocity vector profile on the wall; (c) Partially enlarged view of region I

shown more clearly in Fig. 19c. In the B region, the velocity profile is not uniform, and is mainly caused by the uneven distribution of particles (Fig. 9). The above results are in accord with the simulation (Figs. 9 and 11).

The particle velocities which locate in the sample points (Fig. 15) are acquired through the PIV method, and the comparison is shown in Fig. 20. We find that the simulation results can accurately reflect the variation trend of the particle velocity, and the simulation velocity error is less than 10%. It can also be seen that the PIV result is less than the simulation result. This is mainly caused by the resistance neglected in the simulation.

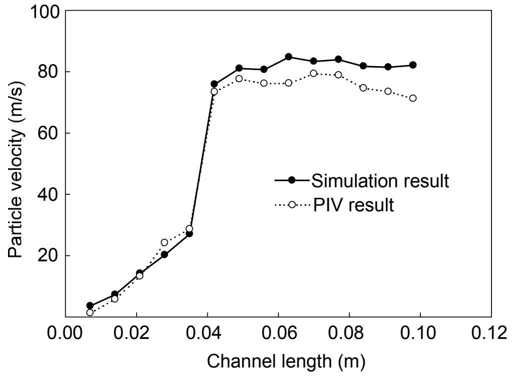

Fig. 20 Comparison of simulation result and experiment result

6 Conclusions

Particle-wall collision occurs in the motion process of a two-phase particle fluid in a finite physical space, and it is a complex liquid-solid coupling matter approximating to a chaotic state. A CFD-DEM modeling approach is proposed, and the main conclusions are as follows.

1. An inter-phase coupling solution method for particle-wall collision is proposed; accurate motion laws of the particle-wall collision process are obtained, and the mechanism of wall contact deformation and material removal can be revealed.

2. The results show that there are radial texture phenomena on the profiles of particle trajectories caused by the flowing interference of the particle fluid; the central region of the flow field has the lowest velocity amplitude, which can be regarded as a rigid core of a Rankine vortex; the injection flux can change the contact point distributions in a finite range; when D=20 mm, the contacting point distribution with rotating superposition reaches the best uniformity; the higher viscosity can carry more particles, and the transporting ability of the fluid medium is improved; in the case of impact flowing, the particle-wall collision pressure and collision velocity increase with the increase of fluid viscosity; if the fluid flowing direction is parallel to the wall, the particle-wall collision pressure and collision velocity mainly depend on the turbulent motion of the fluid, and decrease with the increase of fluid viscosity; the uniform contact effects can be more easily performed by the low viscosity fluid.

3. By means of PIV method, the real particle velocities are obtained, and the effectiveness of the proposed modeling method can be validated.

Modeling and solving for particle-wall collision process have a high level of difficulty. This can not only offer theoretical support for the modeling of multiphase particle fluid, but also can provide technical support for flow regulation of some engineering areas. Future research will examine the facets of multi-field coupling of particle fluid and optimization for a CFD-DEM solution.

References

Cao, Z.C., Cheung, C.F., 2014. Theoretical modelling and analysis of the material removal characteristics in fluid jet polishing. *International Journal of Mechanical Sciences*, **89**:158-166. http://dx.doi.org/10.1016/j.ijmecsci.2014.09.008

Chen, G.J., Zhang, Y.J., Yang, Y.S., 2013. Modelling the unsteady melt flow under a pulsed magnetic field. *Chinese Physics B*, **22**(12):124703. http://dx.doi.org/10.1088/1674-1056/22/12/124703

Gao, H., Guo, L.J., Zhang, X.M., 2002. Liquid–solid separation phenomena of two-phase turbulent flow in curved pipes. *International Journal of Heat and Mass Transfer*, **45**(25):4995-5005. http://dx.doi.org/10.1016/S0017-9310(02)00207-7

Guala, M., Stocchino, A., 2007. Large-scale flow structures in particle-wall collision at low Deborah numbers. *European Journal of Mechanics-B/Fluids*, **26**(4):511-530. http://dx.doi.org/10.1016/j.euromechflu.2006.10.004

Hu, G.M., 2010. Analysis and Simulation of Granular System by Discrete Element Method Using EDEM. Wuhan University of Technology Press, Wuhan, China, p.145-146 (in Chinese).

Ji, S.M., Weng, X.X., Tan, D.P., 2012a. Analytical method of softness abrasive two-phase flow field based on 2D model of LSM. *Acta Physica Sinica*, **61**(1):010205 (in Chinese).

Ji, S.M., Zhong, J.Q., Tan, D.P., 2012b. Distribution and dynamic characteristic of particle group with different concentration in structural flow passage. *Transactions of the Chinese Society of Agricultural Engineering*, **28**(4): 45-53 (in Chinese).

Jin, Y.F., Wan, Y., Zhang, B., *et al.*, 2017. Modeling of the chemical finishing process for polylactic acid parts in fused deposition modeling and investigation of its tensile properties. *Journal of Materials Processing Technology*, **240**:233-239. http://dx.doi.org/10.1016/j.jmatprotec.2016.10.003

Kotrocz, K., Mouazen, A.M., Kerenyi, G., 2016. Numerical simulation of soil-cone penetrometer interaction using discrete element method. *Computers and Electronics in Agriculture*, **125**:63-73. http://dx.doi.org/10.1016/j.compag.2016.04.023

Kowsari, K., Nouraei, H., Samareh, B., *et al.*, 2016. CFD-aided prediction of the shape of abrasive slurry jet micro-machined channels in sintered ceramics. *Ceramics International*, **42**(6):7030-7042. http://dx.doi.org/10.1016/j.ceramint.2016.01.091

Kruggel-Emden, H., Simsek, E., Rickelt, S., 2007. Review and extension of normal force models for the discrete element method. *Powder Technology*, **171**(3):157-173. http://dx.doi.org/10.1016/j.powtec.2006.10.004

Ku, X.K., Lin, J.Z., 2008. Motion and orientation of cylindrical and cubic particles in pipe flow with high concentration and high particle to pipe size ratio. *Journal of Zhejiang University-SCIENCE A*, **9**(5):664-671. http://dx.doi.org/10.1631/jzus.A071463

Li, C., 2012. Study of Near Wall Area Micro-cutting Mechanism and Control Method for Softness Abrasive Flow Finishing. PhD Thesis, Zhejiang University of Technology, Hangzhou, China (in Chinese).

Lopez, A., Nicholls, W., Stickland, M.T., *et al.*, 2015. CFD study of Jet Impingement Test erosion using Ansys Fluent® and OpenFOAM®. *Computer Physics Communications*, **197**:88-95. http://dx.doi.org/10.1016/j.cpc.2015.07.016

Mansouri, A., Arabnejad, H., Karimi, S., *et al.*, 2015. A combined CFD/experimental methodology for erosion prediction. *Wear*, **332**:1090-1097. http://dx.doi.org/10.1016/j.wear.2014.11.025

Nguyen, N.Y., Tian, Y.B., Zhong, Z.W., 2014. Modeling and simulation for the distribution of slurry particles in chemical mechanical polishing. *International Journal of Advanced Manufacturing Technology*, **75**(1):97-106. http://dx.doi.org/10.1007/s00170-014-6132-9

Ren, C.J., Wang, J.D., Song, D., *et al.*, 2011. Determination of particle size distribution by multi-scale analysis of acoustic emission signals in gas-solid fluidized bed. *Journal of Zhejiang University-SCIENCE A (Applied Physics & Engineering)*, **12**(4):260-267. http://dx.doi.org/10.1631/jzus.A1000396

Sun, Q.C., Wang, G.Q., 2009. An Introduction to the Mechanics of Granular Materials. Science Press, Beijing, China, p.33-34 (in Chinese).

Tan, D.P., Zhang, L.B., 2014. A WP-based nonlinear vibration sensing method for invisible liquid steel slag detection. *Sensors and Actuators B: Chemical*, **202**:1257-1269. http://dx.doi.org/10.1016/j.snb.2014.06.014

Tan, D.P., Ji, S.M., Li, P.Y., *et al.*, 2010. Development of vibration style ladle slag detection methods and the key technologies. *Science China Technological Sciences*, **53**(9):2378-2387. http://dx.doi.org/10.1007/s11431-010-4073-6

Tan, D.P., Li, P.Y., Ji, Y.X., *et al.*, 2013. SA-ANN-based slag carry-over detection method and the embedded WME platform. *IEEE Transactions on Industrial Electronics*, **60**(10):4702-4713. http://dx.doi.org/10.1109/TIE.2012.2213559

Tan, D.P., Ji, S.M., Fu, Y.Z., 2015. An improved soft abrasive flow finishing method based on fluid collision theory. *International Journal of Advanced Manufacturing Technology*, **85**(5):1261-1274.

Tan, D.P., Yang, T., Zhao, J., *et al.*, 2016. Free sink vortex Ekman suction-extraction evolution mechanism. *Acta Physica Sinica*, **65**(5):054701 (in Chinese).

Wan, S., Ang, Y.J., Sato, T., *et al.*, 2014. Process modeling and

CFD simulation of two-way abrasive flow machining. *International Journal of Advanced Manufacturing Technology*, **71**(5):1077-1086. http://dx.doi.org/10.1007/s00170-013-5550-4

Wang, T., Wan, Y., Kou, Z.J., *et al*., 2016. Construction of a bioactive surface with micro/nano-topography on titanium alloy by micro-milling and alkali-hydrothermal treatment. *Proceedings of the Institution of Mechanical Engineers, Part H: Journal of Engineering in Medicine*, **230**(12):1086-1095. http://dx.doi.org/10.1177/0954411916675382

Wu, X.C., Wu, Y.C., Zhang, C.C., *et al*., 2013. Fundamental research on the size and velocity measurements of coal powder by trajectory imaging. *Journal of Zhejiang University-SCIENCE A (Applied Physics & Engineering)*, **14**(5):377-382. http://dx.doi.org/10.1631/jzus.A1200233

Zhang, K., Xiong, H.B., Shao, X.M., 2016. Dynamic modeling of micro- and nano-sized particles impinging on the substrate during suspension plasma spraying. *Journal of Zhejiang University-SCIENCE A (Applied Physics & Engineering)*, **17**(9):733-744. http://dx.doi.org/10.1631/jzus.A1500203

中文概要

题　目：液固两相流体中颗粒-壁面冲击碰撞壁面效应研究

目　的： 颗粒-壁面冲击碰撞是近似混沌运动的液固耦合问题。针对传统建模方法难以描述颗粒-壁面碰撞运动过程所涉及的壁面效应问题，本文旨在提出一种液固耦合建模方法，以揭示流固耦合条件下的颗粒-壁面接触规律，探讨碰撞过程中环境变量（流道结构和流体粘度）对碰撞壁面效应的作用机理；得到在约束及非约束空间流场中，流体粘度与颗粒-壁面碰撞行为的内在联系，为流体光整加工、轮机叶片及反应器内壁面磨损所涉及的流场调控提供技术支持。

创新点： 1. 建立适用于液固两相流的计算流体力学和离散单元法（CFD-DEM）耦合动力学模型；2. 通过捕捉颗粒-壁面碰撞点分布，得到不同流道结构及流体粘度下的颗粒-壁面作用范围；3. 建立无量纲化材料去除方程，探明非约束及约束空间流场内流体粘度对材料去除分布的影响。

方　法： 1. 将颗粒视为理想刚体，对流体运动及颗粒运动分别进行建模，通过求解流体对颗粒的作用力以及网格单元内流体体积分数实现两者之间的交互耦合，进而得到流场内颗粒的运动规律；2. 采用软球接触模型描述颗粒-壁面碰撞过程，进而得到不同流道结构及流体粘度下的颗粒-壁面碰撞落点分布；3. 计算颗粒-壁面冲击速度及冲击压力，通过无量纲化材料去除方程，得到约束空间及非约束空间内不同流体粘度下的工件表面材料去除分布。

结　论： 1. 流道结构及流体粘度会极大影响颗粒-壁面碰撞落点分布；在本文算例中，为获得均匀的工件加工效果，应采用较低粘度流体，并使抛光盘做周期性自转运动。2. 随着流体粘度的升高，流体输运颗粒的能力增强，在非约束空间内的颗粒对壁面的碰撞冲击越剧烈，但在约束空间内的碰撞作用力减弱；在本文算例中，为获得更为均匀的材料去除分布，应采用较低粘度流体。3. 借助粒子图像测速法得到了壁面处颗粒速度分布，并与模拟结果进行对比，验证了建模方法的有效性。

关键词： 壁面接触效应；CFD-DEM；颗粒-壁面冲击；两相颗粒流